doi:10.1016/S0022-2836(03)00471-6 J. Mol. Biol. (2003) 329, 551–563

JMB

Available online at www.sciencedirect.com

SCIENCE DIRECT®

The Effects of Mutations on Motions of Side-chains in Protein L Studied by ^{2}H NMR Dynamics and Scalar Couplings

Oscar Millet[1]†, Anthony Mittermaier[1]†, David Baker[2] and Lewis E. Kay[1]*

[1]*Protein Engineering Network Center of Excellence and Departments of Medical Genetics, Biochemistry and Chemistry, University of Toronto, 1 King's College Circle Toronto, Ont., Canada M5S 1A8*

[2]*Department of Biochemistry University of Washington Seattle, WA 98195, USA*

**Corresponding author*

Recently developed ^{2}H spin relaxation experiments are applied to study the dynamics of methyl-containing side-chains in the B1 domain of protein L and in a pair of point mutants of the domain, F22L and A20V. X-ray and NMR studies of the three variants of protein L studied here establish that their structures are very similar, despite the fact that the F22L mutant is 3.2 kcal/mol less stable. Measurements of methyl ^{2}H spin relaxation rates, which probe dynamics on a picosecond–nanosecond time scale, and three-bond $^3J_{C\gamma-CO}$, $^3J_{C\gamma-N}$ and $^3J_{C\alpha-C\delta}$ scalar coupling constants, which are sensitive to motion spanning a wide range of time-scales, reveal changes in the magnitude of side-chain dynamics in response to mutation. Observed differences in the time-scale of motions between the variants have been related to changes in energetic barriers. Of interest, several of the residues with different motional properties across the variants are far from the site of mutation, suggesting the presence of long-range interactions within the protein that can be probed through studies of dynamics.

Keywords: side-chain dynamics; deuterium relaxation; protein stability; site-directed mutagenesis

Introduction

The structural and dynamic properties of proteins are determined by their primary amino acid sequence. Elucidation of the rules that govern this relationship is of immense practical and intellectual importance. Numerous studies have investigated the consequences of changes in protein primary sequence by characterizing the stability, structure and activity of mutant proteins.[1] Far fewer have examined the changes in internal dynamics that accompany amino acid substitutions. Conformational fluctuations modulate distant-dependent energetic interactions, contribute to the entropy of functionally relevant states and can guide enzymatic reaction pathways.[2–4] It is important, therefore, to develop robust methods to study these processes and to understand the relation between protein dynamics and primary sequence.

NMR relaxation experiments are sensitive to protein internal dynamics spanning a wide range of time-scales (extending from seconds to picoseconds) and can pinpoint their location with atomic resolution.[5] Most studies have focused on using ^{15}N spin relaxation as a probe of backbone amide motions in proteins[6] but recently interest has emerged in the study of side-chain dynamics as well.[2] Dynamic analyses of side-chains typically focus on methyl groups, monitoring the decay of ^{13}C or ^{2}H magnetization.[7] Deuterium longitudinal (R_1) and transverse ($R_{1\rho}$) relaxation measurements in fractionally deuterated protein samples have been used to characterize determinants of ligand binding in SH2 domains[8] and RNA–protein complexes,[9] protein stability[10] and hydrophobic core formation in *de novo* protein design.[11] Recently we have extended the number of experimentally accessible deuterium relaxation rates from two (R_1 and $R_{1\rho}$) to a total of five observables.[12] This enables the application of more complicated physical models in the interpretation of the data, allowing, for example, the detection of nanosecond (ns) time-scale motions in side-chains.[13]

† O.M. and A.M. contributed equally to this work.

E-mail address of the corresponding author: kay@pound.med.utoronto.ca

0022-2836/03/$ - see front matter

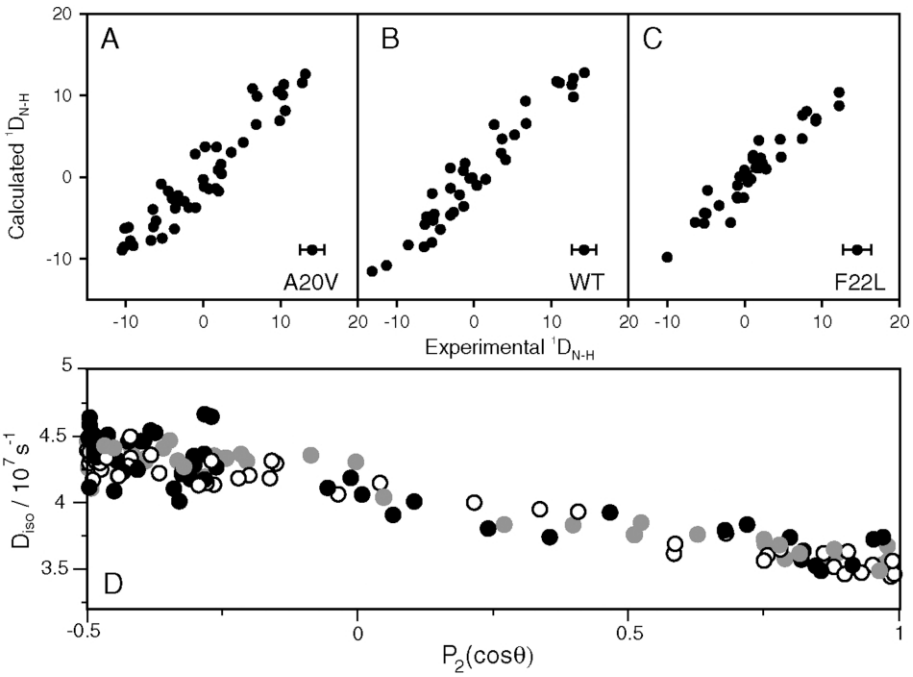

Figure 1. Comparison of $^{15}N-^1H$ residual dipolar couplings predicted on the basis of best-fit alignment frame parameters and the WT crystal structure (1HZ6[41]) with experimental data obtained for the protein L B1 domain (A) A20V, (B) WT and (C) F22L. Experimental uncertainties are indicated by error bars in the bottom right-hand corners of the panels. (D) Plot of D_{iso} *versus* $P_2(\cos\theta)$ (where θ is the angle between an NH bond vector and the unique axis of the diffusion tensor, $P_2(x) = (3x^2 - 1)/2$ for WT (white), A20V (gray) and F22L (black). Extracted values for $1/(6D_{iso})$ are consistent with the presence of purely monomeric species in solution.

We have chosen the wild-type (WT) B1 immunoglobulin binding domain of peptostreptoccocal protein L and two single hydrophobic core mutants, A20V and F22L, as a model system[14] to investigate how single point mutations affect protein internal dynamics with particular emphasis on changes in nanosecond time-scale motions. Examination of the five ^{2}H relaxation rates per methyl group reveals several changes in nanosecond time-scale dynamics in response to the A20V and F22L substitutions. We have performed extensive simulations to better understand the sensitivity of ^{2}H relaxation parameters to motions on multiple time-scales and present some useful guidelines for establishing whether nanosecond time-scale side-chain dynamics are present. This is important, since the present study is among the first that compares side-chain dynamics in a series of mutant proteins and robust protocols for estimating the amplitudes and time-scales of dynamics are, therefore, of particular interest. In addition we report values of three-bond $^3J_{C\gamma-CO}$, $^3J_{C\gamma-N}$ and $^3J_{C\alpha-C\delta}$ scalar coupling constants, which we show can be used in conjunction with ^{2}H relaxation data to place bounds on the time-scale of side-chain motions. We compare the dynamics of A20V, F22L and the WT protein in relation to their molecular structures and recast differences in nanosecond time-scale motions in terms of changes in dihedral angle potential energy functions.

Results and Discussion

The global fold of protein L is unaffected by the mutations A20V, F22L

Equilibrium denaturation experiments show changes in the free energy of unfolding, $\Delta\Delta G_{F,U} = \Delta G^{M}_{F,U} - \Delta G^{WT}_{F,U}$, of 1.23 kcal/mol and −3.22 kcal/mol for A20V (increased stability relative to WT) and F22L (decreased stability), respectively, at 22 °C.[15] Although differences in solvation energy can completely account for the difference in free energy, $\Delta\Delta G_{F,U}$, for A20V (1.24 kcal/mol for A → V)[16] and partially for F22L (−0.12 kcal/mol, F → L)[16] it is still necessary to ascertain to what extent the structures have been modified so that the analysis of the dynamics parameters in what follows (see below) can be interpreted in the proper framework. Crystallographic data show that the structures of A20V and the WT protein are nearly identical (backbone rmsd = 0.5 Å, total rmsd = 1.4 Å; K. Zhang, personal communication). Since a structure of F22L is not available, we have used NMR techniques to assess potential differences from the WT. $^{15}N-^1H$ dipolar couplings are exquisitely sensitive to the orientations of amide bond vectors within the molecular frame, with alterations of the secondary or tertiary structure of the protein reported by large changes in the couplings. Residual amide dipolar couplings measured on all three protein samples show good

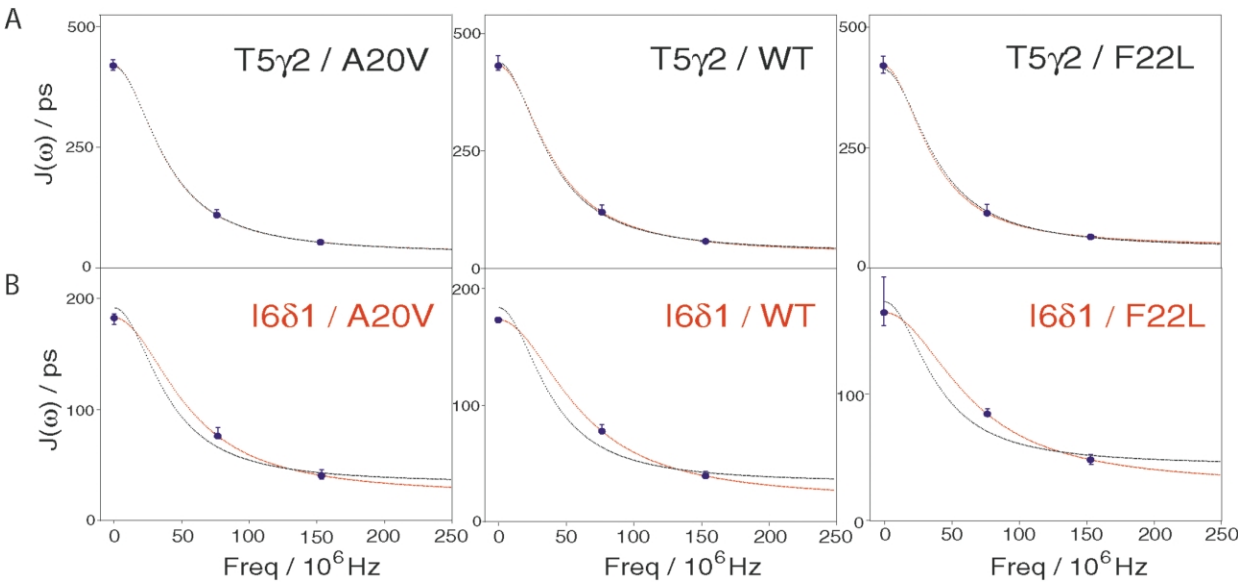

Figure 2. Comparison of spectral density values for T5$^{\gamma 2}$ (A) and I6$^{\delta 1}$ (B), obtained from five deuterium relaxation rates by singular value decomposition[13] (blue circles) with theoretical curves generated assuming a global overall correlation time (black, LS-2 model) and a local correlation time (red, LS-3 model) for the methyl groups in each of the three proteins.

agreement with those predicted from the WT crystal structure (Figure 1A–C), indicating that the overall backbone structures in solution are essentially the same as that of the WT in a crystalline environment. In addition, the hydrodynamic properties of the three molecules were investigated by analysis of backbone ^{15}N relaxation data.[17] The high degree of overlap shown in Figure 1D indicates that all three molecules have very similar diffusion tensors. In addition, methyl regions of ^{13}C–^{1}H correlation maps for WT, A20V and F22L are similar, suggesting that there are no large structural changes of the hydrophobic cores of the proteins. This agrees with numerous studies showing that the average conformation of a protein is remarkably invariant to amino acid substitution, with minimal rearrangement accompanying substitutions of non-native side-chains at both surface and core positions.[18,19]

The backbone ^{15}N relaxation data were used to extract order parameters, reflecting the amplitudes of NH bond vector motions, with a value of 1 (0) corresponding to complete (no) ordering. Order parameter values do not show substantial differences when data for the three molecules are compared (see below), with a large change for only a single residue, L22 (0.87 in WT, 0.75 in F22L). This result is consistent with previous dynamic studies where few significant deviations in the ^{15}N-derived backbone order parameters were found in proteins with altered stability.[20,21]

Side-chain ^{2}H NMR relaxation experiments are sensitive to nanosecond motions

Methyl ^{2}H relaxation experiments were performed on fractionally deuterated, uniformly ^{13}C, ^{15}N labeled protein samples. For spin $I = 1$ nuclei such as deuterium, five independent relaxation rates for three coherences and two populations can be measured by recording a series of ^{13}C–^{1}H correlation experiments.[12] We have measured these five rates for methyl deuterons in each of the three forms of protein L studied (WT, A20V, F22L) at a single field, 500 MHz (^{1}H frequency).

Deuterium relaxation is dominated by the quadrupolar mechanism where only three frequencies (0, ω_D and $2\omega_D$, with ω_D the deuterium resonance frequency) determine the rates of decay of each ^{2}H nucleus. A measure of the "amount" of motion occurring at each frequency, ω, is given by the spectral density function, $J(\omega)$, that corresponds to the cosine Fourier transform of the autocorrelation function describing the time dependence of the orientation of the C–D bond. Since the five relaxation rates depend upon the spectral density function evaluated at frequencies of 0, ω_D and $2\omega_D$, $J(0)$, $J(\omega_D)$ and $J(2\omega_D)$ can be calculated without the assumption of any motional model.[13] It is often instructive, however, to recast the $J(\omega)$ values in terms of site-specific dynamics parameters that reflect the amplitude, S^2, of the motion of the methyl 3-fold axis by fitting the relaxation rates to a model (referred to in what follows as LS-2) of the form:[22,23]

$$J(\omega) = \frac{1}{9} S^2 \frac{\tau_R}{1+\omega^2\tau_R^2} + \left(1 - \frac{1}{9}S^2\right)\frac{\tau}{1+\omega^2\tau^2} \qquad (1)$$

$$\tau^{-1} = \tau_e^{-1} + \tau_R^{-1}$$

where τ_R is the overall tumbling time of the protein determined from ^{15}N relaxation data and τ_e is the effective correlation time for rotations about and motions of the C^{methyl}–C bond.

Figure 2 shows the experimental values of $J(\omega)$

(blue circles) at frequencies (Hz) of 0, $\omega_D/2\pi$ and $2\omega_D/2\pi$ superimposed on the best-fit spectral density curves (black lines) predicted by the LS-2 model for a pair of methyl groups, T5$^{\gamma 2}$ and I6$^{\delta 1}$, from A20V, WT and F22L protein L B1 domains. In the case of T5$^{\gamma 2}$ (Figure 2A) the LS-2 model is able to reproduce the experimental data for all forms of the protein. The dynamics of this methyl group can be adequately described, therefore, in terms of a model in which there is rapid picosecond time-scale rotation about the C$^{\beta}$–C$^{\gamma 2}$ bond, which in turn undergoes rapid librations. In contrast, the LS-2 model cannot reproduce the spectral densities for I6$^{\delta 1}$ (Figure 2(B)). A slightly more complex model (LS-3), in which τ_R is replaced with an effective correlation time $\tau_{R,eff}$, as an additional fitting parameter in equation (1), reproduces the data in this case (red curves) and in all cases for which LS-2 fails. Failure of the LS-2 model can result, in part, from anisotropic overall tumbling. In the present case, however, the range of calculated τ_R values for the methyl groups based on diffusion parameters obtained from ^{15}N relaxation data and the X-ray structure of protein L is small (3.8–4.3 ns; for 23 methyl groups the range is 3.9–4.1 ns)[13] and cannot account for the differences in observed and calculated $J(\omega)$ values. These differences reflect the presence of slower nanosecond time-scale processes (which are not accounted for by the LS-2 model), likely arising from rotameric side-chain jumps around χ_1 and/or χ_2 dihedral angles[13] in addition to the picosecond time-scale dynamics described above. In the LS-3 model, slow motions are incorporated into the effective local correlation time $\tau_{R,eff}$ (if their time-scales are greater than approximately 2 ns) with S^2 and τ_e reflecting motions on the picosecond time-scale.[13,24]

In principle, more complicated models can be used which explicitly take into account the effects of motions on different time-scales. The extended model-free approach (model LS-4) has been used extensively with ^{15}N relaxation data to yield an order parameter (S_s^2) and correlation time (τ_s) per residue describing nanosecond internal motions, in addition to the fast time-scale parameters (S_f^2 and τ_f).[25] In this case the spectral density function is given by:

$$J(\omega) = \frac{1}{9}S_f^2S_s^2\frac{\tau_0}{1+\omega^2\tau_0^2} + \frac{1}{9}S_f^2(1-S_s^2)\frac{\tau_1}{1+\omega^2\tau_1^2}$$
$$+S_s^2\left(1-\frac{1}{9}S_f^2\right)\frac{\tau_2}{1+\omega^2\tau_2^2} + \left(1-\frac{1}{9}S_f^2\right)$$
$$\times(1-S_s^2)\frac{\tau_3}{1+\omega^2\tau_3^2}, \qquad 1/\tau_0 = 1/\tau_R \qquad (2)$$
$$1/\tau_1 = (1/\tau_R) + (1/\tau_s),$$
$$1/\tau_2 = (1/\tau_R) + (1/\tau_f),$$
$$1/\tau_3 = (1/\tau_R) + (1/\tau_s) + (1/\tau_f)$$

In a recent study of side-chain dynamics in WT protein L we found that fits using the LS-4 model of a comprehensive relaxation data set comprised of rates recorded at spectrometer frequencies of 400, 500, 600 and 800 MHz were often unstable in the sense that large errors in the fitting parameters were extracted from the analysis.[13] Subsequent extensive simulations in our laboratory have confirmed that fits of either ^{2}H or ^{13}C-labeled methyl side-chain relaxation parameters using the LS-4 model are not nearly as stable as corresponding analyses of ^{15}N relaxation data, even if extensive data sets (measured at the four spectrometer fields shown above) with small errors (3%) are used as input. The difference in the robustness of backbone and side-chain data analyses arises from the additional factor of 1/9 (which is absent for ^{15}N relaxation data), which significantly decreases the sensitivity of the relaxation data to the dynamics parameters S_s^2, S_f^2 and τ_s.[24] Moreover, simulations have established that the χ^2 values obtained by fitting the five relaxation rates to an LS-4 spectral density model (four parameters) do not follow the distribution expected for one degree of freedom. Note that the five rates are not independent, since they depend on only three spectral density values ($J(0)$, $J(\omega_D)$, $J(2\omega_D)$) and it is therefore not possible to extract four parameters from data obtained at a single spectrometer field. In contrast, fits using LS-2 (two parameters) or LS-3 (three parameters) spectral density models follow the χ^2 distributions expected for three and two degrees of freedom, respectively. Thus, quite independent of the (lack of) robustness of the LS-4 model for fitting methyl dynamics data, it is not valid for use in the present analysis in any event. In what follows, therefore, we will use the LS-3 model in cases where analyses using an LS-2 form of the spectral density function fail.

The "relative goodness of fits" of the five measured relaxation rates/residue using LS-2 and LS-3 models have been analyzed with *F*-test statistics.[26] Simulations of the five ^{2}H relaxation rates that have been measured here (spectrometer field of 500 MHz) using the LS-2 model to generate data free from nanosecond motions have shown, not surprisingly, that when a 95% confidence limit is used to distinguish between LS-2 and LS-3 models, false positives (i.e. selection of the LS-3 model) are obtained in approximately 5% of the cases (data not shown). A related question of interest concerns the efficacy of the *F*-test approach for identifying nanosecond dynamics in cases where such motions exist. To investigate this we turn to simulations again and generate ^{2}H spin relaxation data sets (all five rates at a single spectrometer field, 500 MHz) using the LS-4 model with dynamics parameters in the following ranges, $0.2 < S_f^2 < 1.0$, $0 < S_s^2 < 0.5$, $0 < \tau_f < 100$ ps, $1 < \tau_s < 10$ ns, $3.8 < \tau_R < 4.6$ ns (i.e. all rates derived from a model that includes nanosecond motions). A distribution of overall correlation times, $3.8 < \tau_R < 4.6$ ns, was used in the simulations to reflect the range of τ_R values found in

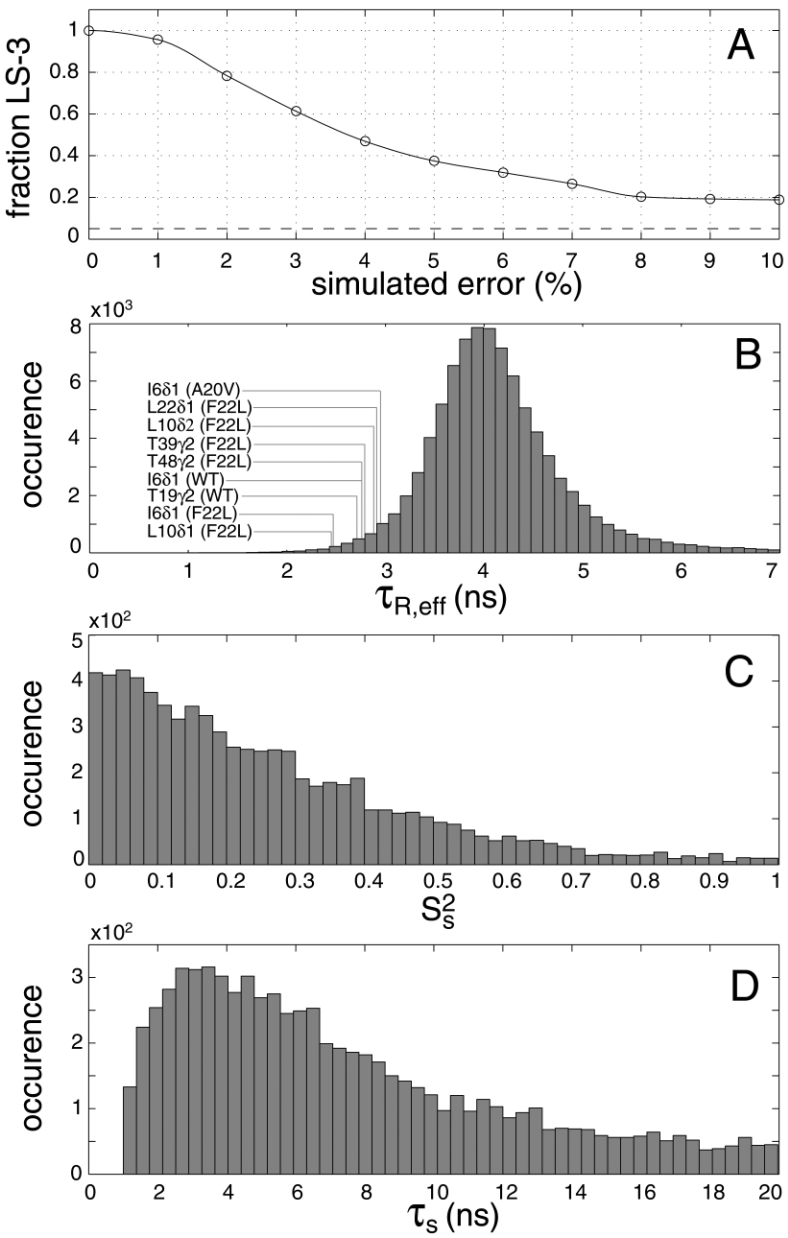

Figure 3. Plot of the fraction of synthetic data sets derived using the LS-4 spectral density model with large amplitude nanosecond dynamics ($S_s^2 < 0.5$) that are better fit with the LS-3 spectral density than the LS-2 (95% confidence limit) *versus* the error in the fitted relaxation rates (see the text for details) (A). Histogram of $\tau_{R,eff}$ values generated from fits using the LS-3 form of $J(\omega)$ to data sets generated with the LS-2 model and the parameters $0.2 < S^2 < 1.0$, $0 < \tau_e < 100$ ps and $3.8 < \tau_R < 4.6$ ns. Values of $\tau_{R,eff}$ for those residues in protein L that are better fit with the LS-3 model than the LS-2 are indicated (B). Histogram of S_s^2 (C) and τ_s (D) values which give $\tau_{R,eff} < 3$ ns and p values < 0.05 in a comparison of LS-2 and LS-3 models when data is generated according to equation (2) with $0.2 < S_f^2 < 1.0$, $0 < S_s^2 < 1.0$, $0 < \tau_f < 100$ ps and $1 < \tau_s < 20$ ns and fit using LS-2 and LS-3 models.

protein L resulting from diffusion anisotropy, $D_{\|}/D_{\perp} = 1.38$ (see Materials and Methods). Gaussian noise was subsequently added to the rates (ranging from 0.01% to 10%) and they were then fit to LS-2 and LS-3 models. Figure 3A shows the fraction of data sets that were better fit with the LS-3 spectral density function (95% confidence limit) *versus* the error in the fitted relaxation rates. For very low errors the majority of residues are correctly identified as having nanosecond motions. As the error increases, however, it becomes increasingly difficult to select the more complex model (LS-3) over LS-2 and many of the residues are undetected (note that all residues should be detected as they all have nanosecond motions in the simulation). Ultimately as the errors increase we expect that the acceptance level will drop to 5% (broken line in the Figure), reflecting simply the 95% cutoff criteria that we use in the *F*-test.

Table 1 lists the methyl groups whose relaxation data could be fit using the simple LS-2 model (95% confidence limit), indicating that the methyl dynamics are well described assuming only picosecond time-scale motions, along with their dynamics parameters. Notably, this Table comprises the majority of methyl-containing residues in each of the three variants of protein L (97% for A20V, 94% for WT and 83% for F22L). Similar levels of nanosecond dynamics have also been observed in ^{2}H relaxation studies of the N-terminal SH3 domain from drk and the fyn SH3 domain where 7% and 21% of the methyl-containing residues, respectively, were better fit using the LS-3 model. Of note, the values of S^2 and τ_e obtained from the fits are very well conserved across the different variants of the protein, with one exception, L40$^{\delta 2}$, where different S^2 and τ_e values are obtained for the A20V mutant. This gives us a

Table 1. Side-chain parameters and scalar couplings

(A) Side-chain dynamical parameters and measured ^3J side-chain scalar couplings for residues whose ^{2}H relaxation rates are best fit using the LS-2 form of $J(\omega)$ (i.e. no nanosecond dynamics)

	S^2(LS-2)[a]			τ_e(LS-2) (ps)[a]				$^3J_{C\alpha-C\delta}$ /(Hz)[a]			$^3J_{C\gamma-N}$ (Hz)[a]			$^3J_{C\gamma-CO}$ (Hz)[a]		
Methyl group	*A20V*	*WT*	*F22L*	*A20V*	*WT*	*F22L*	Rotamer (deg.)[b]	*A20V*	*WT*	*F22L*	*A20V*	*WT*	*F22L*	*A20V*	*WT*	*F22L*
T5$^{\gamma2}$	0.88(0.03)	0.89(0.04)	0.83(0.05)	32(3)	37(3)	45(5)	−60	–	–	–	[c]	[c]	[c]	[c]	[c]	[c]
I6$^{\gamma2}$	0.83(0.07)	0.84(0.03)	0.84(0.06)	29(3)	28(5)	27(7)	−60	–	–	–	1.7(0.1)	1.8(0.1)	1.8(0.1)	1.0(0.1)	1.1(0.1)	1.1(0.1)
I11$^{\gamma2}$	0.73(0.04)	0.77(0.04)	0.74(0.02)	34(6)	29(5)	30(3)	−60	–	–	–	1.8(0.1)	1.9(0.1)	1.7(0.1)	0.5(0.1)	0.5(0.1)	0.6(0.1)
I11$^{\delta1}$	0.42(0.02)	0.40(0.02)	0.40(0.02)	23(3)	22(3)	24(3)	180	3.0(0.1)	3.0(0.1)	3.2(0.2)	–	–	–	–	–	–
A13	0.90(0.02)	0.83(0.03)	0.84(0.07)	33(2)	37(4)	49(5)	–	–	–	–	–	–	–	–	–	–
T17$^{\gamma2}$	[c]	0.57(0.06)	[c]	[c]	68(5)	[c]	+60	–	–	–	[c]	[c]	[c]	[c]	[c]	[c]
A20	–	0.82(0.05)	[c]	[c]	58(5)	[c]	–	–	–	–	–	–	–	–	–	–
V20$^{\gamma1}$	0.61(0.03)	–	–	35(3)	–	–	180	–	–	–	0.9(0.1)	–	–	2.3(0.1)	–	–
V20$^{\gamma2}$	0.29(0.02)	–	–	50(3)	–	–	180	–	–	–	1.1(0.1)	–	–	1.9(0.1)	–	–
T25$^{\gamma2}$	0.87(0.02)	0.84(0.06)	0.83(0.03)	39(2)	40(7)	43(3)	+60	–	–	–	0.8(0.1)	0.6(0.1)	0.7(0.1)	3.2(0.1)	3.4(0.2)	3.4(0.2)
A29	0.88(0.02)	0.89(0.04)	0.76(0.11)	75(2)	82(5)	79(13)	–	–	–	–	–	–	–	–	–	–
T30$^{\gamma2}$	0.99(0.08)	0.91(0.07)	0.86(0.12)	31(7)	44(9)	41(9)	−60	–	–	–	1.9(0.1)	1.9(0.1)	1.8(0.1)	0.3(0.2)	0.4(0.2)	0.6(0.2)
A33	0.82(0.02)	0.84(0.02)	0.86(0.09)	81(4)	75(4)	53(5)	–	–	–	–	–	–	–	–	–	–
A35	0.86(0.03)	0.84(0.02)	0.86(0.07)	62(3)	50(5)	49(4)	–	–	–	–	–	–	–	–	–	–
A37	0.86(0.04)	0.90(0.10)	0.90(0.11)	126(5)	125(12)	121(10)	–	–	–	–	–	–	–	–	–	–
L40$^{\delta1}$	0.53(0.14)	0.56(0.17)	0.54(0.16)	30(12)	36(12)	29(5)	180	3.2(0.1)	3.0(0.2)	3.0(0.2)	–	–	–	–	–	–
L40$^{\delta2}$	0.25(0.01)	0.47(0.03)	0.54(0.03)	79(1)	41(2)	35(3)	180	0.9(0.1)	0.9(0.1)	0.8(0.1)	–	–	–	–	–	–
V49$^{\gamma1}$	0.67(0.04)	0.62(0.03)	0.60(0.05)	51(2)	54(3)	53(4)	+60	–	–	–	0.4(0.1)	0.3(0.1)	0.3(0.2)	0.9(0.1)	1.0(0.1)	0.9(0.2)
V49$^{\gamma2}$	0.76(0.03)	0.69(0.06)	0.62(0.07)	77(5)	80(4)	84(5)	+60	–	–	–	1.5(0.1)	1.6(0.2)	1.7(0.2)	0.5(0.2)	0.8(0.1)	0.6(0.1)
V51$^{\gamma1}$	0.73(0.05)	0.68(0.03)	0.72(0.04)	31(3)	35(4)	35(4)	180	–	–	–	1.8(0.1)	1.8(0.1)	1.8(0.1)	0.9(0.1)	0.5(0.1)	0.6(0.1)
V51$^{\gamma2}$	0.65(0.03)	0.64(0.03)	0.62(0.04)	37(2)	37(2)	37(3)	180	–	–	–	0.4(0.1)	<0.2	0.4(0.2)	3.3(0.2)	3.2(0.1)	3.2(0.2)
A52	0.83(0.03)	0.84(0.03)	0.85(0.03)	24(2)	24(4)	24(3)	–	–	–	–	–	–	–	–	–	–
T57$^{\gamma2}$	0.97(0.02)	0.97(0.05)	[c]	50(3)	56(8)	[c]	−60	–	–	–	[c]	[c]	[c]	[c]	[c]	[c]
L58$^{\delta1}$	0.59(0.12)	0.65(0.11)	0.65(0.09)	58(7)	67(5)	52(9)	180	3.9(0.2)	3.9(0.2)	3.8(0.2)	–	–	–	–	–	–
L58$^{\delta2}$	0.61(0.02)	0.62(0.04)	0.65(0.03)	39(2)	38(3)	43(4)	180	<0.2	<0.2	<0.2	–	–	–	–	–	–
I60$^{\gamma2}$	0.86(0.05)	0.83(0.04)	0.75(0.06)	23(6)	26(5)	28(2)	−60	–	–	–	1.8(0.1)	1.9(0.1)	1.8(0.1)	0.9(0.1)	1.0(0.1)	1.0(0.1)
I60$^{\delta1}$	0.57(0.01)	0.61(0.02)	0.57(0.02)	18(2)	14(3)	19(3)	180	3.6(0.1)	3.7(0.1)	3.6(0.1)	–	–	–	–	–	–

(B) Predicted values for the different types of long range ^3J scalar couplings as a function of the dihedral angle

		Scalar coupling (Hz)					Scalar coupling (Hz)					Scalar coupling (Hz)		
Type of scalar coupling	Methyl type	$\chi_{+60°}$	$\chi_{180°}$	$\chi_{-60°}$	Type of scalar coupling	Methyl type	$\chi_{+60°}$	$\chi_{180°}$	$\chi_{-60°}$	Type of scalar coupling	Methyl type	$\chi_{+60°}$	$\chi_{180°}$	$\chi_{-60°}$
$^3J_{C\gamma-N}$[d]	Val$^{\gamma1}$/ Val$^{\gamma2}$	0.4/2.1	2.1/0.4	0.4/ 0.4	$^3J_{C\gamma-CO}$[d]	Val$^{\gamma1}$/ Val$^{\gamma2}$	0.6/0.6	0.6/3.6	3.6/0.6	$^3J_{C\alpha-C\delta}$[e]	Leu$^{\delta1}$	≤1.2	>3	≤1.2
	Thr$^{\gamma2}$	0.2	0.2	1.9		Thr$^{\gamma2}$	3.4	0.4	0.4		Leu$^{\delta2}$	>3	≤1.2	≤1.2
	Ile$^{\gamma2}$	0.4	0.4	2.1		Ile$^{\gamma2}$	3.6	0.6	0.6		Ile$^{\delta1}$	≤1.2	>3	≤1.2

[a] Errors in experimental data in parentheses.
[b] Rotamers obtained from the crystal structures: 1HZ5 and 1HZ6.[41]
[c] Data not available due to signal overlap.
[d] Predicted scalar couplings according to a Karplus parametrization with coefficients obtained from Perez *et al.*[30]
[e] Large values for $^3J_{C\alpha-C\delta}$ correspond to *trans* conformations, whereas small values of the scalar coupling correspond to *gauche* conformations.[29]

high degree of confidence in our data and suggests strongly that when differences do arise in relaxation parameters they are very likely real. In addition to the ^{2}H spin relaxation data reported here, we also show the three-bond scalar couplings[27,28] $^3J_{C\alpha-C\delta}$, $^3J_{C\gamma-N}$ and $^3J_{C\gamma-CO}$ that have been measured for methyl-containing residues and used as a probe of χ_1/χ_2 dynamics to complement the relaxation measurements (see below).

Notably, several methyl groups (six in F22L, two in WT and one in A20V) in protein L show strong evidence of nanosecond time-scale dynamics from ^{2}H spin relaxation measurements. For these residues the LS-2 model is unable to reproduce the experimental spectral density values to within error and all residues show a statistically significant reduction in residual χ^2 from fits using the LS-3 model relative to LS-2 according to *F*-statistics (95% confidence limit). Table 2 lists the dynamics parameters, S^2 and $\tau_{R,eff}$, that are extracted from fits (LS-3) of the residues that show nanosecond motions in at least one of the three forms of protein L that are studied here (highlighted in bold). In addition, the three-bond scalar couplings $^3J_{C\alpha-C\delta}$, $^3J_{C\gamma-N}$ and $^3J_{C\gamma-CO}$ are also listed. Of interest, the results in Figure 3A suggest that with the level of errors in our experimental data sets (ranging from approximately 2% for A20V and WT to 4–7% for F22L) it is unlikely that all residues with nanosecond time-scale dynamics will be identified, with less than 50% in the case of F22L. In cases where nanosecond motions are detected, however, the simulations described below suggest that they likely arise from large amplitude dynamics ($S_s^2 < 0.6$).

It can be shown that $\tau_{R,eff}$ values obtained from fitting the data to the LS-3 model are quite sensitive to the presence of nanosecond motions,[13] provided that the magnitude of fast internal motions does not overwhelm the effect of overall tumbling. Figure 3B shows the distribution of $\tau_{R,eff}$ values obtained from LS-3 fits of synthetic data generated using the LS-2 form of $J(\omega)$ (no nanosecond time-scale dynamics) with $0.2 < S^2 < 1.0$, $0 < \tau_e < 100$ ps and $3.8 < \tau_R < 4.6$ ns, along with the $\tau_{R,eff}$ values obtained for those residues in protein L identified as dynamic on the nanosecond time-scale by *F*-tests. The distribution is centered about $\tau_{R,eff} \sim 4$ ns, since $\tau_{R,iso} = 4.05$ ns and 97% of the values lie to the right of 3 ns. Note that the width of the distribution is larger than the range of τ_R values used in the simulation, since experimental errors are also included (see Materials and Methods). For residues with nanosecond dynamics it is quite clear that lower $\tau_{R,eff}$ values than would be expected (less than 3 ns for protein L) in the absence of nanosecond dynamics are obtained. Low values of $\tau_{R,eff}$ are very informative in terms of providing insight into the underlying dynamics. By way of example, we have simulated ^{2}H relaxation data using the LS-4 spectral density model (i.e. with nanosecond time-scale dynamics) with $0.2 < S_f^2 < 1.0$, $0 < S_s^2 < 1.0$, $0 < \tau_f < 100$ ps, $1 < \tau_s < 20$ ns and $3.8 < \tau_R < 4.6$ ns and fit the

Table 2. Side-chain dynamical parameters and measured ^3J side-chain scalar couplings for residues whose ^{2}H relaxation are best fit using the LS-3 form of $J(\omega)$ in at least one variant of protein L (i.e. nanosecond dynamics)

Methyl group	S^2(LS-3)[a]	$\tau_{R,eff}$ (ns)[a]	Rotamer (deg.)[b]	$^3J_{C\alpha-C\delta}$ (Hz)[a]	$^3J_{C\gamma-N}$ (Hz)[a]	$^3J_{C\gamma-CO}$ (Hz)[a]
A20V						
I6$^{\delta 1}$[c]	**0.49(0.04)**	**2.95(0.16)**	**−60**	**1.9(0.1)**	–	–
L10$^{\delta 1}$	0.24(0.03)	3.25(0.15)	180	2.4(0.1)	–	–
L10$^{\delta 2}$	0.26(0.06)	3.12(0.14)	180	2.0(0.1)	–	–
T19$^{\gamma 2}$	0.52(0.08)	3.76(0.05)	+60	–	0.8(0.1)	2.1(0.2)
T39$^{\gamma 2}$	0.86(0.05)	4.01(0.12)	+60	–	0.8(0.1)	2.2(0.1)
T48$^{\gamma 2}$	0.75(0.03)	3.76(0.17)	+60	–	[d]	[d]
WT						
I6$^{\delta 1}$[c]	**0.49(0.03)**	**2.76(0.10)**	**−60**	**2.1(0.2)**	–	–
L10$^{\delta 1}$	0.21(0.04)	3.38(0.20)	180	2.3(0.1)	–	–
L10$^{\delta 2}$	0.26(0.02)	2.83(0.22)	180	1.8(0.1)	–	–
T19$^{\gamma 2}$[c]	**0.82(0.04)**	**2.71(0.18)**	**+60**	**–**	**0.9(0.1)**	**2.0(0.2)**
T39$^{\gamma 2}$	0.87(0.03)	3.56(0.12)	+60	–	0.8(0.1)	2.2(0.2)
T48$^{\gamma 2}$	0.75(0.03)	3.73(0.15)	+60	–	1.1(0.1)	3.1(0.2)
F22L						
I6$^{\delta 1}$[c]	**0.47(0.07)**	**2.47(0.17)**	**−60**	**1.9(0.2)**	–	–
L10$^{\delta 1}$[c]	**0.17(0.03)**	**2.45(0.13)**	**180**	**1.7(0.1)**	–	–
L10$^{\delta 2}$[c]	**0.29(0.04)**	**2.88(0.09)**	**180**	**2.0(0.1)**	–	–
T19$^{\gamma 2}$	0.57(0.03)	3.22(0.07)	+60	–	0.7(0.1)	2.2(0.1)
L22$^{\delta 1}$[c]	**0.50(0.06)**	**2.91(0.18)**	**–**	**2.2(0.2)**	–	–
L22$^{\delta 2}$	0.69(0.07)	2.17(0.12)	–	2.0(0.1)	–	–
T39$^{\gamma 2}$[c]	**0.95(0.08)**	**2.79(0.10)**	**+60**	**–**	**1.1(0.1)**	**2.1(0.1)**
T48$^{\gamma 2}$[c]	**0.72(0.03)**	**2.76(0.14)**	**+60**	**–**	**0.9(0.1)**	**1.9(0.1)**

[a] Errors in experimental data in parentheses.
[b] Rotamers obtained from the crystal structures: 1HZ5 and 1HZ6.[41]
[c] Residues identified as dynamic using *F*-test statistics (see the text).
[d] Data not available due to signal overlap.

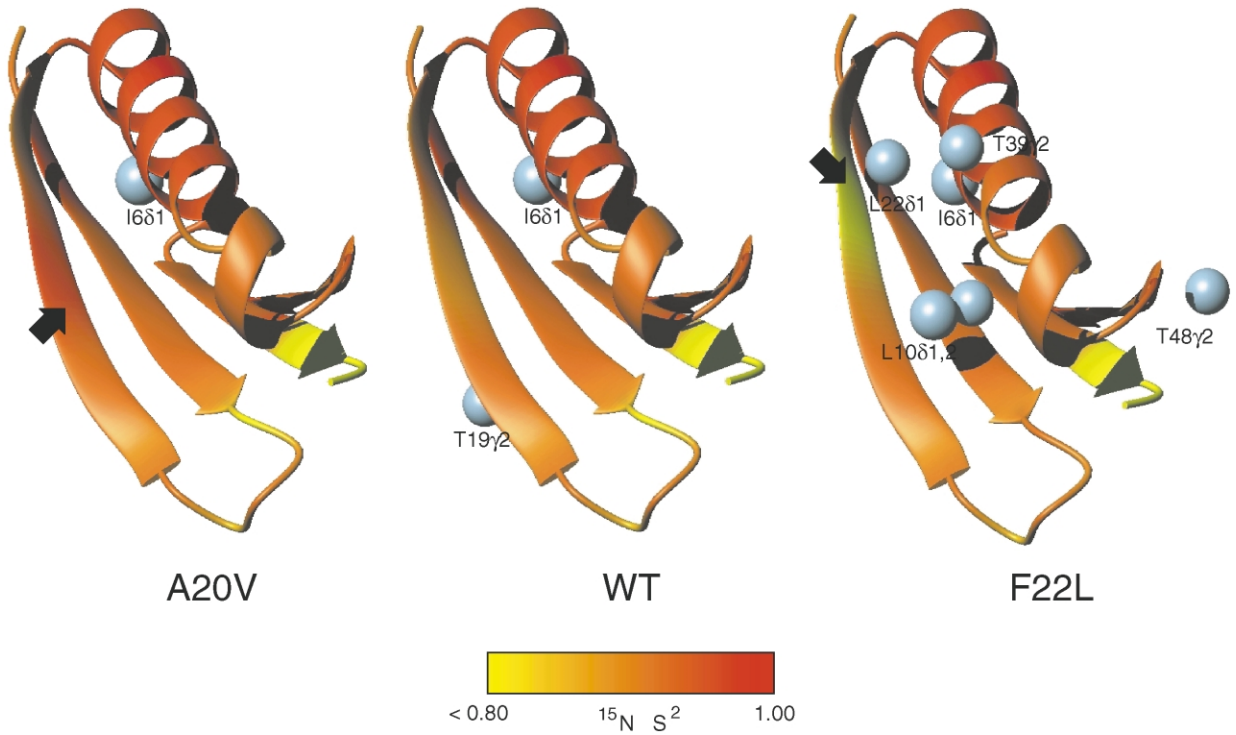

Figure 4. Structure of the B1 domain of protein L (PDB accession code 1HZ6[41]) with the locations of methyl groups undergoing nanosecond motions indicated by gray beads. The backbone ribbon is colored according to ^{15}N order parameter where yellow and red correspond to regions of higher and lower flexibility, respectively. Black arrows indicate the sites of mutation.

rates to both LS-2 and LS-3 spectral density models. The input values of S_s^2 and τ_s for those cases where the LS-3 model is preferred (*F*-test, 95% confidence) and where $\tau_{R,eff} < 3$ ns are plotted in Figure 3C and D, respectively. For $\tau_{R,eff} < 3$ ns the distribution of τ_s lies predominantly in the range of 1–10 ns (75%). Moreover, the values of S_s^2 are clustered from 0 to 0.6 (92%) and show no correlation with the input values of τ_s. Note that the definition of "low values of $\tau_{R,eff}$" (in what follows we use less than 3 ns for protein L) will vary depending on the protein, but can be easily calculated on a case-by-case basis using simulations of the type described here.

The methyl-containing residues identified as dynamic on a nanosecond time-scale in Table 2 are superimposed on the structure of protein L in Figure 4. In addition, the amplitudes of backbone motions, established from ^{15}N spin relaxation measurements, are color coded on the ribbon diagrams of each structure. It is clear that there are essentially no differences in backbone order. In contrast, however, differences in the numbers of residues showing side-chain nanosecond dynamics are observed. Of note, the I6$^{\delta 1}$ methyl is the only one that displays nanosecond motions in all three forms of the protein. L10$^{\delta 1,\delta 2}$ are selected as dynamic on a nanosecond time-scale in the case of F22L but not WT or A20V (see Table 2). In the case of L10$^{\delta 1}$ the probability of a chance improvement in fit using the LS-3 *versus* LS-2 form of $J(\omega)$ is 83% ($p = 0.83$) for WT and 90% ($p = 0.90$) for A20V and the separation between "nanosecond dynamics" and "no nanosecond dynamics" is relatively clear. Such a separation is much less clear for L10δ2, where p values of 0.17 and 0.25 are obtained for WT and A20V, respectively. Values of p from fits of T19, T39 and T48 for (F22L, WT, A20V) are (0.69,0.02,0.75), (0.03,0.87,0.90) and (0.04,0.75,0.85) respectively, and we can be reasonably confident here that residues not selected by the LS-3 model are unlikely to be dynamic on a nanosecond time-scale. It is important to emphasize the distinction on the one hand between establishing the presence of nanosecond motions (for example, using the *F*-test criterion described above) and establishing the absence of nanosecond dynamics for those residues that do not pass the *F*-test criterion.

Correlation with scalar coupling data

In addition to measuring deuterium spin relaxation parameters, three-bond $^{13}C^{\alpha}-^{13}C^{\delta}$, $^{13}C^{\gamma}-^{13}CO$ and $^{13}C^{\gamma}-^{15}N$ scalar coupling constants[27,28] were obtained for all three variants of protein L and are reported in Tables 1 and 2. These values depend directly on the dihedral angles χ_2 ($^3J_{C\alpha-C\delta}$) and χ_1 ($^3J_{C\gamma-CO}$, $^3J_{C\gamma-N}$) and can be used to detect rotameric averaging on time-scales ranging from a few hundredths of a second to picoseconds.[29] Also included in Table 1 are the expected scalar couplings for dihedral angles of ±60 and 180°.[30] With the exception of V20, the measured scalar coupling

values reported in Table 1 are consistent with a single predominant χ_1/χ_2 rotamer in all three variants of protein L examined. For these residues the ^{2}H relaxation data are well fit using the LS-2 spectral density model (i.e. absence of nanosecond time-scale dynamics) and the χ_1/χ_2 angles obtained on the basis of the scalar coupling data are in agreement with those from the X-ray structures of the protein. For V20 the $^3J_{C\gamma-CO}$ couplings, in particular, indicate averaging. Of interest, the order parameters for the γ1 and γ2 positions are very different; since motions that involve only rotations about χ_1 would lead to equal order parameters, the dynamics are more complex at this site.

All residues with detected nanosecond motions (highlighted in red in Table 2) give values of scalar couplings that are consistent with either extensive averaging about the relevant dihedral angles (χ_1 or χ_2) or, much less likely, non-staggered dihedral angle values. The complementarity between scalar coupling and deuterium relaxation measurements is well illustrated by the data for T48 (see Table 2). In the WT protein, $^3J_{C\gamma-CO}$ and $^3J_{C\gamma-N}$ coupling constants are equal to 3.1 Hz and 1.1 Hz, respectively, corresponding to the +60 rotamer. A previous analysis of dipolar couplings showed a small degree of χ_1 averaging for this residue with the −60 rotamer populated to approximately 15%.[31] The experimental $^3J_{C\gamma-N}$ coupling constant in the WT protein is consistent with some exchange between the +60 and −60 rotamers, however, in F22L, values of 1.9 Hz and 0.9 Hz for $^3J_{C\gamma-CO}$ and $^3J_{C\gamma-N}$, respectively, are diagnostic of more extensive dynamics. Moreover, the ^{2}H data strongly support the fact that only in the case of F22L are large amplitude nanosecond time-scale dynamics present for this residue. The source of these dynamics is almost certainly rotation about χ_1 and it seems likely, therefore, that the motion that contributes to the additional averaging of the scalar couplings in T48,F22L is in the nanosecond regime.

Many of the residues for which averaged scalar coupling values are measured also display nanosecond time-scale dynamics from analysis of ^{2}H spin relaxation rates. Conspicuous exceptions from Table 2 include T39 in A20V,WT and T19 in A20V,F22L. In the case of T39, scalar coupling values indicate significant averaging in all forms of the protein. However, only in the case of the F22L variant does the LS-2 model fail in the analysis of the relaxation data for this residue. Similarly for T19 only the WT protein shows nanosecond dynamics using the criteria outlined above, yet the values of the scalar couplings indicate averaging in all variants. It is important to note, however, that there need not be a correlation between the presence of nanosecond time-scale dynamics (as monitored by spin relaxation measurements) and averaging as reported by scalar couplings. For example, the simulations described above show that the "window" in which ^{2}H relaxation experiments can detect slow motions according to *F*-test statistics and $\tau_{R,eff}$ values below 3 ns is quite sensitive to the motional time-scale. In the present case, values of $\tau_{R,eff}$ below 3 ns, extracted for all of the residues selected as dynamic on the nanosecond time-scale (Table 2), indicate that the underlying dynamics likely involve large amplitudes and time-scales between approximately 1 ns and 10 ns (see Figure 3C and D). In contrast, averaged scalar couplings can reflect motions over a much wider time-scale. In this way torsion angle dynamics with time constants that lie outside the 1–10 ns window (Figure 3D) would escape detection by ^{2}H spin relaxation (sensitive only to picosecond to nanosecond motions) and yet would efficiently average scalar coupling constants.

Thus, the presence of dynamics that average scalar couplings but not relaxation parameters can be used to set boundaries regarding the time-scale of averaging. In the case of T39 the extensive averaging detected by scalar couplings in A20V and WT likely is the result of motions on time-scales greater than 10 ns so that the dynamics are invisible to ^{2}H spin relaxation, yet they must be fast enough to avoid spectral broadening (millisecond time-scale). The nanosecond motions reported for T39 by the ^{2}H data in the case of F22L but not for A20V or WT may reflect additional intra-rotameric dynamics superimposed on the slower torsion angle jumps that the averaged scalar coupling data report. Alternatively, the effect of the F22L mutation may be to increase the rate of the rotameric jumps in the first place so that they are shifted into the nanosecond regime. Since the evidence from NMR experiments and molecular dynamics simulations is that librations within a rotameric well occur on the picosecond time-scale[32] we tend to favor the second scenario listed above. Of note, values of S^2 are similar for all three variants, suggesting that the amplitudes of fast (ps) dynamics are similar in the three cases.

The measured scalar couplings for T19, like for T39, are consistent with extensive χ_1 averaging. In this case, however, the relaxation data are only conclusive about nanosecond dynamics at this position in the WT protein (see Table 2). Notably, the S^2 value (reporting on picosecond dynamics) is high for the WT (0.82) and significantly lower for both mutants (0.52 and 0.57 for A20V and F22L), possibly resulting from a shift in averaging for T19 from the nanosecond regime for WT to the picosecond time frame for the mutants.

Comparison with molecular structures

Analysis of the X-ray structures of A20V and WT establishes that the residues that show differential picosecond and nanosecond time-scale motions in the three proteins (L10, T19, T39, L40, T48) do not make direct contacts with the mutated residues. It is therefore of interest to try to understand the structural features that might be responsible for the changes in dynamics associated with amino acid substitutions. For example, T39 is far from the site of mutation in F22L (>10 Å) and yet

substantial changes in nanosecond motions are observed for this residue in F22L relative to the other forms of the protein. In both WT and A20V rotameric averaging of T39 occurs on a relatively slow time-scale, greater than approximately 10 ns. Of interest, in both WT and A20V X-ray structures (an X-ray structure of the F22L mutant is not available) the hydroxyl group T39 proton is favorably located to form a hydrogen bond with the backbone carbonyl oxygen atom of Y36 ($H^{\gamma 1}$–O distance $\approx$1.7 Å, $O^{\gamma 1}$–$H^{\gamma 1}$–O angle of 6°). The increase in the rate of T39 rotameric averaging in F22L may therefore be due to slight changes in tertiary structure relative to A20V and WT that disrupt this interaction, by increasing either the $H^{\gamma 1}$–O separation or the $O^{\gamma 1}$–$H^{\gamma 1}$–O angle.

In the cases of T19 and T48, no partners for side-chain hydrogen bonding are apparent from the WT and A20V X-ray structures. It has been shown, however, that the rotamer populations of a mobile surface residue depend to a large extent upon its intra-residue backbone conformation[33] and it may be that the energetic barriers separating rotameric states are also sensitive to backbone geometry. The A20V and WT X-ray structures establish that there is a greater than 30° difference in the ψ dihedral angle of T19 in the two forms of the protein, which may well affect the χ_1 dynamics of this residue. T19 is not the only residue to show significant changes in local backbone conformation. Six φ and ψ angles differ by more than 30° between A20V and WT, and the overall φ/ψ dihedral angle pairwise rmsd is of the order of 15°. It is likely, therefore, that the increase in T48 side-chain dynamics observed for F22L is related to a similar local backbone conformational readjustment.

The order parameter, S^2, reflecting picosecond time-scale motions of L40$^{\delta 2}$ in A20V, is significantly reduced compared to its corresponding values in F22L and WT. The order parameter of L40$^{\delta 1}$, however, is the same in all three proteins, suggesting that the additional dynamics detected by L40$^{\delta 2}$ are highly anisotropic, occurring mainly about an axis of rotation parallel with the C^{γ}–$C^{\delta 1}$ bond vector. The side-chain of L40 is packed against the hydrophobic core of the protein, at a distance of almost 10 Å from A20 in the WT structure. A comparison of A20V and WT X-ray structures shows small displacements ($\leq$1 Å) in side-chains contacting L40, in particular those of L10, I60 and Y36. Although these conformational changes are quite minor, the structural determinants of fast time-scale side-chain motions are not well understood,[34] and local structural rearrangement likely mediates the effect of the A20V mutation on L40 dynamics. Similarly small structural perturbations may be responsible for the nanosecond time-scale motions detected for L10 only in F22L and not in A20V or WT.

Analysis in terms of energetic barriers

Changes in local energetics associated with shifts in the time-scales of rotameric jumps can be estimated using the phenomenological Arrhenius equation:

$$k_{ij} = A \exp\{ - \Delta G_t/RT\} \quad (3)$$

where k_{ij} is the first-order rate constant describing transitions from rotamer i to rotamer j, ΔG_t is the difference in free energy between the transition state and rotamer i, R is the universal gas constant, T is the temperature in Kelvin and the value of A is system-dependent. An exact knowledge of A is not required to assess the kinetic effects of changes in barrier height that result from a point mutation, for example, so long as it does not change between the variants, since:

$$\Delta\Delta G_t = RT \ln\{k_A/k_B\} \quad (4)$$

where k_A and k_B are the rates for the same rotameric transition in proteins A and B and $\Delta\Delta G_t = \Delta G_t^B - \Delta G_t^A$. As described above, in the case of protein L simulations have established that the ^{2}H spin relaxation data are sensitive to slow time-scale dynamics extending from approximately 1–10 ns so long as $\tau_{R,eff} < 3$ ns. Thus, for T39 where nanosecond dynamics are observed only in F22L and where averaging about χ_1 does take place in all three variants (established by the scalar couplings), the motional time-scale must change by at least an order of magnitude between F22L and the other two forms of the protein. This corresponds to a change in barrier height of at least 1.3 kcal/mol between A20V/WT and F22L for this residue.

The value of the prefactor, A, must be known to calculate the absolute heights of the energetic barriers between conformational states. According to Eyring theory, $A = kT/h$, where k and h are Boltzmann's and Planck's constants, respectively. Rate constants obtained for serine and threonine residues in a 50 ns molecular dynamics simulation of the N-terminal SH3 domain from drk are in good agreement with equation (3), using barrier heights from the trajectory and with A set to the Eyring prefactor. Accordingly, a value of $\Delta G_t = 5.6$ kcal/mol gives a first order rate constant of 5×10^8 s^{-1} (2 ns time constant) at 298 K, providing a rough estimate of the free energy barriers that could produce the nanosecond time-scale motions detected here.

Conclusions

Here, we have used newly developed ^{2}H spin relaxation measures in concert with three-bond scalar coupling data to investigate how the dynamics of side-chain methyl groups change in response to mutation. The increase in stability of the A20V mutant may be completely rationalized in terms of the hydrophobicity difference between alanine and valine residues, and its structure is essentially identical with that of the WT protein. It is not surprising, therefore, that the dynamic

properties are rather conserved, although T19 does show large changes in order parameters between A20V/F22L and WT, and L40$^{\delta 2}$ displays larger amplitude dynamics in A20V than in the other two variants. In contrast, the destabilization of F22L is significantly greater than what would be predicted from the modest difference in hydrophobicity between phenylalanine and leucine residues. Here too, however, dipolar couplings establish that at least globally the structure does not change. Since there is a greater potential for disruption of specific favorable interactions in the folded state relative to its unfolded counterpart, it is probable that the loss of stability derives largely from an increase in the free energy of the folded state. Combined thermal and guanidine denaturation analyses show that this destabilization is primarily enthalpic (not shown). Nonetheless, as described above, there are some quite significant changes in side-chain dynamics between WT and F22L. Notably, many of the residues affected are quite distant (>10 Å for T48 and T39, for example) from the site of mutation, indicating the presence of long-range conformational coupling to F22. This is perhaps not surprising given the highly cooperative nature of protein folding. This study establishes the utility of ^2H spin relaxation experiments to detect and characterize motions on the nanosecond and picosecond time-scales. The methodology is particularly useful in concert with other measures that are sensitive to dynamics, such as scalar couplings, and together these two approaches can be used to obtain insight into how mutations affect the magnitudes and time scales of internal motions in proteins.

Materials and Methods

Sample preparation and NMR spectroscopy

DNA sequences encoding the three variants of the B1 domain of peptostreptoccocal protein L (all with the Y45W substitution) were sub-cloned into pET11d vectors (Novagen) as described elsewhere.[31] Freshly transformed *Escherichia coli* BL21 DE3 cells were used to obtain protein samples. Protein expression was induced in isotopically enriched media containing 50% ^2H_2O, with $^{15}NH_4Cl$ and [^{13}C]glucose as the sole sources of nitrogen and carbon. Partial alignment of samples was achieved through the addition of 10 mg/ml Pf1 bacteriophage[35] and dipolar couplings were recorded using HSQC-IPAP spectra.[36,37] Methyl spectra were assigned using standard multidimensional multinuclear NMR experiments.[38] Stereospecific assignments of the methyl groups of valine and leucine were obtained using the method of Neri *et al.*[39] All relaxation data were recorded on samples comprising ~1 mM protein (pH 6.0), 50 mM Na_3PO_4, 25 °C on a Varian Inova spectrometer (500 MHz ^1H frequency).

Data analysis and model selection

Parameters for each molecule describing the magnitude (A_a), anisotropy (A_r) and orientation (α,β,γ) of molecular alignment[40] were fit to $^{15}N-^1H$ dipolar couplings collected for A20V, F22L, and WT samples using the WT (1HZ6[41]) X-ray structure and in-house software. Dipolar couplings were predicted based on the best-fit alignment parameters and the orientations of NH bond vectors in the 1HZ6 structure. Local diffusion constants were calculated from ^{15}N R_1 and $R_{1\rho}$ relaxation rates and fit to an axially symmetric global diffusion tensor using the program quadric.[17] Other models of molecular tumbling were not justified on the basis of *F*-test statistics. The relaxation rates obtained from the five ^2H relaxation experiments were shown to be self-consistent using methods described previously.[12] The isotropic correlation time ($\tau_R = 1/(6D_{iso})$) extracted from the ^{15}N relaxation analysis was used to fit the five deuterium relaxation rates from each methyl group employing a standard model-free approach[23,22] (LS-2) yielding residual χ^2_{LS2} values, $\chi^2_{LS2} = \sum(R_i^{expt} - R_i^{calc})^2/\sigma_i^2$, for each methyl group with R_i^{calc} given by equation (1) of Millet *et al.* [12] It is noteworthy that only very small changes are obtained in extracted dynamics parameters when τ_R values calculated for each methyl based on the orientation of the $C^{methyl}-C$ axis with respect to the diffusion frame are used instead of $1/(6D_{iso})$[13] (for the extreme case of Ala61, S^2 changes from 0.60 to 0.65). The LS-2 spectral density functions (shown in black in Figure 2) are obtained by inserting the fitted dynamics parameters into equation (1). Deuterium relaxation data were additionally fit using the same equations with the correlation time optimized on a per methyl group basis (LS-3) yielding residual χ^2_{LS3} values (resultant spectral density functions shown in red). An *F*-test was used to determine the statistical significance of the additional local parameter for each methyl group according to $F = (\chi^2_{LS2} - \chi^2_{LS3})/(\chi^2_{LS3}/2)$, noting that the LS-2 and LS-3 models have three and two degrees of freedom, respectively. The five ^2H relaxation rates were also used to calculate unique sets of three spectral density function values ($J(0)$, $J(\omega_D)$, $J(2\omega_D)$) using singular value decomposition, with error bars for the spectral density values determined from jacknife simulations where a single relaxation rate was excluded from each iteration, as described previously.[13] Values of $J(0)$, $J(\omega_D)$ and $J(2\omega_D)$ obtained in this manner are shown for T5$^{\gamma 2}$ and I6$^{\delta 1}$ in Figure 2.

Simulations

All calculations were performed using MATLAB software (The MathWorks, Inc., Natick, MA, USA). To obtain ranges of $\tau_{R,eff}$ values consistent with the absence of nanosecond motions (Figure 3(B)), the five ^2H relaxation rates were generated according to equation (1) (LS-2 model, 500 MHz spectrometer field) with random values of S^2 and τ_e varying uniformly from 0.2 to 1 and 0 to 100 ps, respectively. The value of τ_R used in each simulation was calculated from the relation $\tau_R = 1/\{6D_{iso} - (3\cos^2\theta - 1)(D_{\|} - D_{\perp})\}$ with $(D_{iso}, D_{\|}, D_{\perp}) = (4.1, 5.0, 3.7) \times 10^7\ s^{-1}$ and with the value of $\cos\theta$ varied uniformly between 0 and 1. Random noise with a Gaussian profile was added to the simulated data using standard deviations corresponding to the mean errors in the experimental measurements for F22L (1.01, 1.80, 1.34, 3.08, 1.15) s^{-1} for decay of the (D_z, D_+, $(3D_z^2 - 2)$, $(D_+D_z + D_+D_z + D_+D_z)$, D_+^2) operators (errors of 3.6, 2.9, 5.6, 6.8, 6.3%, respectively). The resulting rates were subsequently fit with $\tau_{R,eff}$ included as an adjustable parameter replacing τ_R (i.e. LS-3 model). The process was repeated 100,000 times to generate the distribution shown in Figure 3B. In order to investigate what values of S_s^2 and

τ_s are likely to be associated with nanosecond dynamics detected from fits of data involving the LS-3 model additional data sets were simulated using the LS-4 spectral density (equation (2)), with $0.2 < S_f^2 < 1.0$, $0.0 < S_s^2 < 1.0$, $0 < \tau_f < 100$ ps, $1 < \tau_s < 20$ ns. The data sets were fit to both LS-2 and LS-3 models, with the input values of S_s^2 and τ_s illustrated for those cases where p values <0.05 and $\tau_{R,eff}$ values <3.0 ns are obtained (Figure 3C and D): 100,000 simulations were performed, as above.

Acknowledgements

This work was supported by a grant from the Canadian Institutes of Health Research. O.M. is the recipient of an EMBO post-doctoral fellowship. L.E.K. holds a Canada Research Chair in Biochemistry. The authors thank Dr Regis Pomes (Hospital for Sick Children, Toronto) for useful discussions and for kindly making available his 50 ns molecular dynamics trajectory of an SH3 domain and Dr Rhea Hudson (Hospital for Sick Children, Toronto) for help with cloning.

References

1. Brannigan, J. A. & Wilkinson, A. J. (2002). Protein engineering 20 years on. *Nature Rev. Mol. Cell Biol.* **3**, 964–970.
2. Wand, A. J. (2001). Dynamic activation of protein function: a view emerging from NMR spectroscopy. *Nature Struct. Biol.* **8**, 926–931.
3. Eisenmesser, E. Z., Bosco, D. A., Akke, M. & Kern, D. (2002). Enzyme dynamics during catalysis. *Science*, **295**, 1520–1523.
4. Hammes-Schiffer, S. (2002). Impact of enzyme motion on activity. *Biochemistry*, **41**, 13335–13343.
5. Ishima, R. & Torchia, D. A. (2000). Protein dynamics from NMR. *Nature Struct. Biol.* **7**, 740–743.
6. Kay, L. E., Torchia, D. A. & Bax, A. (1989). Backbone dynamics of proteins as studied by ^{15}N inverse detected heteronuclear NMR spectroscopy: application to staphylococcal nuclease. *Biochemistry*, **28**, 8972–8979.
7. Kay, L. E. (1998). Protein dynamics from NMR. *Nature Struct. Biol. NMR*, **5 (suppl.)** 513–517.
8. Kay, L. E., Muhandiram, D. R., Wolf, G., Shoelson, S. E. & Forman-Kay, J. D. (1998). Correlation between binding and dynamics at SH2 domain interfaces. *Nature Struct. Biol.* **5**, 156–163.
9. Mittermaier, A., Varani, L., Muhandiram, D. R., Kay, L. E. & Varani, G. (1999). Changes in side chain and backbone dynamics identify determinants of specificity in RNA recognition by human U1A protein. *J. Mol. Biol.* **294**, 967–979.
10. Lee, A. L. & Wand, A. J. (2001). Microscopic origins of entropy, heat capacity and the glass transition in proteins. *Nature*, **411**, 501–504.
11. Walsh, S. T. R., Lee, A. L., DeGrado, W. F. & Wand, A. J. (2001). Dynamics of a de novo designed three-helix bundle protein studied by ^{15}N, ^{13}C and ^{2}H NMR relaxation methods. *Biochemistry*, **40**, 9560–9569.
12. Millet, O., Muhandiram, D. R., Skrynnikov, N. R. & Kay, L. E. (2002). Deuterium spin probes of side-chain dynamics in proteins. 1. Measurement of five relaxation rates per deuteron in ^{13}C-labeled and fractionally ^{2}H-enriched proteins in solution. *J. Am. Chem. Soc.* **124**, 6439–6448.
13. Skrynnikov, N. R., Millet, O. & Kay, L. E. (2002). Deuterium spin probes of side-chain dynamics in proteins. 2. Spectral density mapping and identification of nanosecond time-scale side-chain motions. *J. Am. Chem. Soc.* **124**, 6449–6460.
14. Scalley, M. L., Yi, Q., Gu, H., McCormack, A., Yates, J. R. & Baker, D. (1997). Kinetics of folding of the IgG binding domain of peptostreptococcal protein L. *Biochemistry*, **36**, 3373–3382.
15. Kim, D., Gu, H. & Baker, D. (1998). The sequences of small proteins are not extensively optimized for rapid folding by natural selection. *Proc. Natl Acad. Sci. USA*, **95**, 4982–4986.
16. Fauchere, J. L. & Pliska, V. (1983). Hydrophobic parameters pi of amino acid side chains from the partitioning of *N*-acetyl amino acid amides. *Eur. J. Med. Chem.* **18**, 369–375.
17. Lee, L. K., Rance, M., Chazin, W. J. & Palmer, A. G. (1997). Rotational diffusion anisotropy of proteins from simultaneous analysis of ^{15}N and ^{13}C$^{\alpha}$ nuclear spin relaxation. *J. Biomol. NMR*, **9**, 287–298.
18. Bowie, J. U., Reidhaar-Olson, J. F., Lim, W. & Sauer, R. T. (1990). Deciphering the message in protein sequences. *Science*, **247**, 1306–1310.
19. Eriksson, A. E., Baase, W. A., Zhang, X. J., Heinz, D. W., Blaber, M., Baldwin, E. P. & Matthews, B. W. (1992). Response of a protein structure to cavity-creating mutations and its relation to the hydrophobic effect. *Science*, **255**, 178–183.
20. Mulder, F. A. A., Hon, B., Muhandiram, D. R., Dahlquist, F. W. & Kay, L. E. (2000). Flexibility and ligand exchange in a buried cavity mutant of T4 lysozyme studied by multi-nuclear NMR. *Biochemistry*, **39**, 12614–12622.
21. Johnson, E. C., Lazar, G. A., Desjarlais, J. R. & Handel, T. M. (1999). Solution structure and dynamics of a designed hydrophobic core variant of ubiquitin. *Structure*, **7**, 967–976.
22. Lipari, G. & Szabo, A. (1982). Model-free approach to the interpretation of nuclear magnetic relaxation in macromolecules: 2. Analysis of experimental results. *J. Am. Chem. Soc.* **104**, 4559–4570.
23. Lipari, G. & Szabo, A. (1982). Model-free approach to the interpretation of nuclear magnetic relaxation in macromolecules: 1. Theory and range of validity. *J. Am. Chem. Soc.* **104**, 4546–4559.
24. Choy, W. Y. & Kay, L. E. (2003). Model selection for the interpretation of protein side chain methyl dynamics. *J. Biomol. NMR*. In the press.
25. Clore, G. M., Szabo, A., Bax, A., Kay, L. E., Driscoll, P. C. & Gronenborn, A. M. (1990). Deviations from the simple 2 parameter model free approach to the interpretation of ^{15}N nuclear magnetic relaxation of proteins. *J. Am. Chem. Soc.* **112**, 4989–4991.
26. Zar, J. H. (1984). Two-sample hypotheses. In *Biostatistical Analysis*, pp. 122-150 Prentice-Hall, Englewood Cliffs, NJ.
27. Bax, A., Max, D. & Zax, D. (1992). Measurement of long-range ^{13}C–^{13}C *J* couplings in a 20-kDa protein–peptide complex. *J. Am. Chem. Soc.* **114**, 6923–6925.
28. Vuister, G. W., Wang, A. C. & Bax, A. (1993). Measurement of three-bond nitrogen–carbon *J* couplings in proteins uniformly enriched in ^{15}N and ^{13}C. *J. Am. Chem. Soc.* **115**, 5334–5335.

29. Bax, A., Vuister, G. W., Grzesiek, S., Delaglio, F., Wang, A. C., Tschudin, R. & Zhu, G. (1994). Measurement of homo- and heteronuclear *J* couplings from quantitative *J* correlation. *Methods Enzymol.* **239**, 79–105.
30. Perez, C., Lohr, F., Ruterjans, H. & Schmidt, J. M. (2001). Self-consistent Karplus parametrization of ^3J couplings depending on the polypeptide side-chain torsion χ_1. *J. Am. Chem. Soc.* **123**, 7081–7093.
31. Mittermaier, A. & Kay, L. E. (2001). χ_1 torsion angle dynamics in proteins from dipolar couplings. *J. Am. Chem. Soc.* **123**, 6892–6903.
32. Bremi, T., Bruschweiler, R. & Ernst, R. R. (1997). A protocol for the interpretation of side-chain dynamics based on NMR relaxation: application to phenylalanines in antamanide. *J. Am. Chem. Soc.* **119**, 4272–4284.
33. Clore, G. M. & Kuszewski, J. (2002). χ^1 rotamer populations and angles of mobile surface side chains are accurately predicted by a torsion angle database potential of mean force. *J. Am. Chem. Soc.* **124**, 2866–2867.
34. Mittermaier, A., Kay, L. E. & Forman-Kay, F. D. (1999). Analysis of deuterium relaxation-derived methyl axis order parameters and correlation with local structure. *J. Biomol. NMR*, **13**, 181–185.
35. Hansen, M. R., Mueller, L. & Pardi, A. (1998). Tunable alignment of macromolecules by filamentous phage yields dipolar coupling interactions. *Nature Struct. Biol.* **5**, 1065.
36. Ottiger, M., Delaglio, F. & Bax, A. (1998). Measurement of *J* and dipolar couplings from simplified two dimensional NMR spectra. *J. Magn. Reson.* **131**, 373–378.
37. Yang, D. & Nagayama, K. (1996). A sensitivity-enhanced method for measuring heternuclear long-range coupling constants from the displacement of signals in two 1D subspectra. *J. Magn. Reson. ser. A*, **118**, 117–121.
38. Bax, A. (1994). Multidimensional nuclear magnetic resonance methods for protein studies. *Curr. Opin. Struct. Biol.* **4**, 738–744.
39. Neri, D., Szyperski, T., Otting, G., Senn, H. & Wüthrich, K. (1989). Stereospecific nuclear magnetic resonance assignments of the methyl groups of valine and leucine in the DNA-binding domain of the 434 repressor by biosynthetically directed fractional ^{13}C labeling. *Biochemistry*, **28**, 7510–7516.
40. Tjandra, N. & Bax, A. (1997). Direct measurement of distances and angles in biomolecules by NMR in a dilute liquid crystalline medium. *Science*, **278**, 1111–1114.
41. O'Neill, J. W., Kim, D. E., Baker, D. & Zhang, K. Y. J. (2001). Crystal structure of the B1 domain of protein L from *Peptostreptococcus magnus* with a tyrosine to tryptophan substitution. *Acta Crystallog. sect. D*, **57**, 480.

Edited by P. Wright

(Received 20 December 2002; received in revised form 26 March 2003; accepted 1 April 2003)